J Nanostruct 12(1): 45-61, Winter 2022

RESEARCH PAPER

Laser and Solar Light-Induced Degradation of Pollutant Dyes Using Bi-Plasmonic Ag-Au Nanoparticles-Decorated Magnetic TiO_2 for Textile Wastewater Treatment

Azizollah Nezhadali [1,2], *Mahmoud Reza Shapouri* [1], *Mitra Amoli-Diva* [3*]

[1] *Department of Chemistry, Payame Noor University (PNU), Mashhad, Iran*

[2] *Department of Chemistry, Payame Noor University, Tehran 19569, Iran*

[3] *Department of Physics, Sharif University of Technology, Tehran, Iran*

ARTICLE INFO

Article History:
Received 28 July 2021
Accepted 12 December 2021
Published 01 January 2022

Keywords:
Ag-Au bi-metallic nanoparticles
Laser enhanced deactivation
Magneto-plasmonic TiO_2
Photodegradation
Textile wastewater

ABSTRACT

Eight eco-friendly, and magnetically-separable heterogeneous photocatalysts including five Au nanoparticles (NPs) modified magnetic TiO_2@Fe_3O_4 NPs and three Ag-Au bi-plasmonic NPs-decorated TiO_2@Fe_3O_4 NPs with enhanced photocatalytic performance under visible light were synthesized and used for photodegradation of methyl orange (MO) as a model pollutant in textile wastewater samples. The photocatalytic activity was assessed using two radiation sources namely, an intense linear 532-nm laser and a continuous solar-simulated xenon lamp. Compared to the TiO_2 alone, the prepared photocatalysts revealed efficient photocatalytic activity in visible region due to the presence of two localized surface plasmon resonance (LSPR)-generated hot electrons from excited Au and Ag NPs and reached to about 98% in 60 min. In addition, the results demonstrated that the photocatalysts have different degradation performance with respect to the type of applied light sources and also to the composition/shell thickness of plasmonic layer. The Langmuir-Hinshelwood adsorption model was used for evaluation of kinetics, degradation rate and half-life time of the reaction and it was concluded that the mechanism of MO degradation involves charge transfer and plasmon resonance energy transfer (PRET) from these plasmonic NPs to the TiO_2. On the other hand, the reusability studies revealed that the photocatalysts can be re-used for several cycles without losing its performance with a convenient magnetic separability. Finally, it is shown that the prepared photocatalysts is successfully applied for degradation of organic pollutant in real textile wastewater.

How to cite this article
Nezhadali A, Shapouri M. R, Amoli-Diva M . PLaser and Solar Light-Induced Degradation of Pollutant Dyes Using Bi-Plasmonic Ag-Au Nanoparticles-Decorated Magnetic TiO_2 for Textile Wastewater Treatment. J Nanostruct, 2022; 12(1):45-61. DOI: 10.22052/JNS.2022.01.006

INTRODUCTION

In the last few years, photocatalytic degradation method has attracted extensive attention as a promising approach for decomposition of hazardous materials excreted from industries, research labs and households due to its convenient, high efficiency and low-cost handling [1, 2]. Within various catalyst Materials, titanium dioxide (TiO_2) is a promising, inexpensive and eco-friendly semiconductor widely used in photocatalytic

* *Corresponding Author Email: amoli@physics.sharif.ir*

applications because of its light-induced oxidation property, chemical stability and non-toxicity [3, 4]. The photo-excited electrons, which are produced under radiation of UV light can promote from the semiconductor's filled-valence band (V_B) to the empty conduction-band (C_B) to generate electron (e^-)/hole (h^+) pairs and the absorbed energy (hv) must be equal or exceed the band gap of TiO_2 [5, 6]. The produced h^+ can react with adsorbed H_2O molecule to form hydroxyl ($OH^•$) radical, while the e^- can react with O_2 molecule to generate superoxide ($O_2^{•}$) radical. Both radicals are highly reactive and can oxidize organic pollutants resulting degradation of them [7].

On the other hand, the morphology of semiconductor can highly affects on its photocatalytic efficiency and larger specific surface area can provide more reactive sites which results the increasing of the catalytic activity [8-12]. Thus, nano-structured TiO_2, especially nanoparticles (NPs) have been replaced in the corresponding catalytic investigations. However, free-standing nano-structured TiO_2 is difficult to separate from the environment due to the complicated separating procedures needed [13] and its composites with a magnetic core which produce functional core-shell structures can be the most promising way to give this semiconductor the potential of applications in different research area including catalysis [14]. In other word, covering TiO_2 NPs onto a Fe_3O_4 NPs core is a facile way to recycle this material because superparamagnetic systems can be conveniently collected, separated, or fixed by applying an external supermagnet [15-19]. Moreover, charge and spin transfer can occur at the interface of magnetic surface/catalytic-active companion resulting in more adjustment of their catalytic properties [14].

Another point of using TiO_2 as a photocatalyst is that wide band gap (3.2 eV) and high recombination rate of the produced charge carriers bring significant limitations to the successful application of this material for photo-conversion processes [18, 19]. A new strategy to improve its photo-response can be decoration of metal nanoparticles (NPs) into the TiO_2 core [20]. It is already known that under UV irradiation in semiconductor alone, the photo-generated electrons are accumulated in $C_{B,}$ while in the metal-semiconductor structure, the photo-produced electrons are transferred from semiconductor to metal [21, 22]. Among metal NPs, plasmonic NPs exhibit localized surface plasmon resonances in visible (Vis) and near-infrared (NIR) wavelengths due to the collective motion of free conduction electrons induced by the electric field of incident light when irradiated by specific wavelength called plasmon wavelength. With UV radiation, the promoted electrons which are in the C_B of TiO_2 is subsequently captured by plasmonic NPs which have a lower energy Fermi level than the C_B potential of TiO_2, resulting in separation of e^-/h+ pairs and an increase of the photo-catalytic efficiency [23, 24]. While, when exposure by visible light, electron transfer from the excited plasmonic metal nanostructure into the semiconductor occurs because the system exhibited photocurrent under excitation of the plasmon band [25, 26] and electron deficiency on plasmonic NPs is in favor of oxidation of organic compounds [27]. Furthermore, integration of these NPs into TiO_2 results in increasing of light absorption in the Vis- NIR region and reduction of recombination rate of photo-generated charge carriers [28, 29]. Au NPs are predominantly used plasmonic particles for many applications because of convenient synthesis procedure, resistance to oxidation, flexible conjugation with other materials, biocompatibility and well-defined localized surface plasmon resonance (LSPR) absorbance. Therefore, our first idea was evaluating $Au@TiO_2@Fe_3O_4$ NPs as an efficient and environmental-friendly recoverable photocatalyst for degradation of organic pollutant from wastewater samples. The second idea was using bimetallic plasmonic NPs as doping materials for further expanding of the absorption band gap of TiO_2 to increase absorption efficiency in Vis region resulting more improve photocatalytic degradation efficiency. In bimetallic plasmonic core-shell systems with small shell thickness, strong LSPR broadening can occur due to the decay into e^-/h^+ pairs via scattering at metal-metal interfaces (the so-called Landau damping) [30]. In addition, increasing in dipolar coupling between NPs with decreasing of particle spacing, provides an additional absorption on the long wavelength side of the spectrum and broadening their optical response [31].

In this study, eight photocatalysts, including five $Au@TiO_2@Fe_3O_4$ NPs and three $Ag\text{-}Au@TiO_2@Fe_3O_4$ NPs with different shell thickness were successfully synthesized by coupling of chemical co-precipitation, thermal-vapor and laser-assisted reduction techniques and characterized using UV-Vis spectroscopy, transmission electron

microscopy (TEM), scanning electron microscopy (SEM), X-ray diffraction (XRD) and vibrating sample magnetometer (VSM). The photocatalytic properties of the prepared nanocatalysts were examined using methyl orange (MO) dye as a model pollutant under radiation of an intense 532-nm laser and a solar-simulated xenon light sources. The kinetic property, degradation rate constant, and half-life time of the reactions were evaluated using Langmuir-Hinshelwood adsorption model. Finally, the prepared photocatalysts were successfully applied for degradation of organic pollutant in real textile wastewater.

MATERIALS AND REAGENTS

All reagents and chemicals were of analytical grade and used as received without further purifications and Millipore water was used throughout the experiments. Ferric chloride, hexahydrate ($FeCl_3.6H_2O$), ferrous chloride tetrahydrate ($FeCl_2.4H_2O$), sodium chloride, tetrabutyl titanate (TBT), gold (III) chloride trihydrate ($HAuCl_4.3H_2O$), polyvinylpirrolidone (PVP), silver nitrate, methyl orange (MO), acetic acid, ammonia solution (25% w/w), ethanol and methanol were purchased from Merck Company (Darmstadt, Germany). All glassware was cleaned with an aqua regia solution (3:1, HCl: HNO_3) and rinsed several times with deionized water prior to use.

Photocatalysts preparation

Synthesis of Fe_3O_4 NPs

Fe_3O_4 NPs was synthesized by one of the most practical and useful methods of NPs synthesis namely, chemical co-precipitation using iron chloride salts in alkaline medium [32]. Briefly, $FeCl_3.6H_2O$ (5.84 g) and $FeCl_2.4H_2O$ (2.15 g) were dissolved in deionized water (150 mL) in a tri-necked round-bottom flask while the temperature was increased to 85 ºC with vigorous stirring. The reaction was performed under N_2 gas flow to prevent NPs from oxidation. After 5 min, ammonia solution (20 mL, 25% w/w) was added to the mixture immediately and the color was changed from orange to black. The suspension was stirred for 10 min under these conditions and then, it was cooled down to the room temperature, and washed sequentially with deionized water (150 mL, twice), 0.02 M sodium chloride (100 mL, once) and ethanol (50 mL, twice). At each washing step, the supernatant was decanted by applying a supermagnet in the bottom of the flask. The sodium chloride solution was used for the flocculation of magnetic NPs and it can accelerate the magnetic separation, particularly in alkaline solutions [33]. Finally, an appropriate amount of ethanol was added to precipitate to reach final density of 50 mg mL^{-1} and it was used as a seed material for deposition of TiO_2 layer.

Synthesis of $TiO_2@Fe_3O_4$ NPs

The $TiO_2@Fe_3O_4$ (TF) core-shell NPs were synthesized by direct coating of TiO_2 layer on the surface of Fe_3O_4 NPs via a vapor-thermal method reported in the literature with some modifications (18). Briefly, 2.0 mL of the above-prepared Fe_3O_4 NPs, 0.5 mL of ammonia solution and 10 mL of TBT (20% v/v in ethanol) were transferred in ethanol (15 mL) and dispersed with sonication for 10 min. This mixture was then transferred to a 50 mL beaker and placed into an autoclave with a 100-mL Teflon-liner container. The free space between the Teflon-liner container and the beaker was filled with deionized water and the sample was heated to 150 °C for 10 h. During this time, vaporized deionized water contacts with TBT and hydrolyzes it. Finally, the sample was cooled down to the room temperature and after magnetically-assisted decantation the obtained precipitate was sequentially washed with deionized water (100 mL, two times) and ethanol (100 mL, two times), and then dried at 50 °C in a vacuum oven for 4 h. Finally, the dried precipitate was calcined at 500 °C for 2 h to improve particles crystallinity.

Synthesis of Au NPs@$TiO_2@Fe_3O_4$ NPs

A laser-assisted reduction technique was used to produce plasmonic magnetic TiO_2 photocatalysts as reported previously in the literature with some modifications [34]. Briefly, 0.2 g of the above prepared TF NPs was transferred into a 25-mL beaker containing gold (III) chloride trihydrates (10 mL, 5.0 mM) and PVP (5 mL, 0.37% w/w in methanol) and placed on the top a shaker. A pulsed Nd:YAG laser with 10 ns pulse width, 130 mJ per pulse intensity, 4 mm beam diameter and 10 Hz repetition rate was used to irradiate the colloidal solutions at 532 nm. The suspension was irradiated by 1000 pulses and labeled as GTF1. In order to have more Au shell thickness, another TF NPs suspension was prepared accordingly and labeled as GTF2 and treated with 2000 pulses. The procedure was continued up to 5000 pulses for

GTF5. To obtain LSPR data, an amount of 500 µL of each colloidal solution was separated from the suspension and transferred into a quartz cell for UV/Vis analysis. Then, the suspensions were dried in a vacuum oven at 50 ºC for 8 h.

Synthesis of Ag-Au NPs@TiO_2@Fe_3O_4 NPs

To prepare bi-plasmonic NPs, three GTF5 samples labeled as SGTF1, SGTF2 and SGTF3 which were all transferred to a 20-mL beaker and 5.0 mL of silver nitrate solution (5 mM) was added to the suspension with vigorous stirring. Then, the numbers of 500, 1000 and 1500 pulses were applied to the samples, respectively. The color of suspensions was gradually changed to brown which confirms the formation of bi-plasmonic Ag-Au@TiO_2@Fe_3O_4 NPs. The prepared photocatalysts were separated from the solutions by magnetically-assisted decantation, washed three times with deionized water (50 mL) and dried in a vacuum oven at 50 ºC for 8 h.

Characterization of the photocatalysts

A wavelength and irradiance-calibrated AvaSpec3648 spectrometer from Avantes company (Apeldoorn, Netherlands) equipped with two 400 µm optical fibers, a CUV-VAR-UV/VIS cuvette holder and an AvaLight DH-S deuterium-halogen light source were applied for measuring UV-Vis spectra. The size and morphology of the prepared photocatalysts were characterized by a Zeiss EM900 transmission electron microscope (TEM) (Oberkochen, Germany) with accelerating voltage of 100 kV and a Hitachi S-4160 scanning electron microscope (SEM) (Tokyo, Japan). Phase characterization of the nanocatalysts was performed using a PANalytical X'Pert PRO MPD X-ray diffractometer (XRD) (Eindhoven, Netherlands) with X'Pert High Score Plus (V.3) software. The magnetization measurement of magnetic particles was carried out by an AGFM/VSM 3886 vibrating sample magnetometer (VSM) (Kashan, Iran) at room temperature.

Photocatalytic studies

Time-dependent photocatalytic properties of the as-synthesized GTF1 to GTF5, and SGTF1 to SGTF3 photocatalysts were evaluated by monitoring degradation of MO aqueous solution in a set of 50-mL beaker containing reaction slurry. The slurry was prepared by adding 50 mg of each photocatalyst to a 30 mL of 6×10^{-5} M of MO solution at pH 4. An intense 532 nm diode laser with the intensity of 630 mW cm^{-2} and a high-pressure xenon lamp (150 W) equipped with a cutoff filter for blocking the UV light (<400 nm) were used as the light sources and placed 10 cm away from the reaction vessels. Prior to the photocatalytic experiments, the slurries were stirred in a dark place with a mechanical shaker for 30 min to ensure complete dye adsorption on the photocatalysts. A beaker containing the same aliquot of MO solution in the absence of any photocatalyst was taken as a reference.

The photocatalytic reaction was induced by turning the laser/xenon lamp on and at each predetermined time interval, an aliquot (500 µL) of aqueous solution was sampled after applying a supermagnet to remove the suspended photocatalyst particles. The absorption spectra of the MO solution were observed at wavelength of 464 nm and its concentration was determined using a pre-constructed calibration curve. Similar experiments were repeated at different pH in the range of 2-9 to obtain optimum pH value for the reaction.

The degradation residue (DR%) of MO was calculated using the following equation:

$$DR\% = \frac{C}{C_0} \times 100 \quad (1)$$

Where, C and C_0 are the concentration of remaining MO at each time interval and initial MO concentration, respectively.

In order to evaluate the reusability and long-term photocatalytic activity, GTF5 and SGTF3 photocatalysts were applied to degrade MO solutions for five consecutive times. Briefly, after irradiation of dye solutions with the 532 nm laser or xenon light sources (for GTF5 and SGTF3, respectively) in 60 min, the magnetic photocatalysts were separated by an external supermagnet, washed twice with 25 mL methanol and trice with 25 mL deionized water and dried at 50 ºC for 8 h. The recovered photocatalysts were subsequently used to degrade fresh MO solutions under the same irradiation conditions mentioned above. The experiments were performed for five consecutive cycles with the same procedure.

Kinetics of the photocatalytic reaction

Most of the photocatalytic reactions follow the Langmuir-Hinshelwood adsorption model and this model can be simplified to a pseudo-first order

equation [35, 36]:

$$ln\frac{C_0}{C} = kt \quad (2)$$

Where, k is the photocatalytic reaction rate constant and can be calculated from the slop of linear plot of ln (C_0/C) versus t for each photocatalyst.

In addition, for the pseudo first order reaction, the half-life time ($t_{1/2}$) obtains from the below equation [35]:

$$t_{\frac{1}{2}} = \frac{ln2}{k} \quad (3)$$

The rate constant and half-life time of each photodegradation reaction were evaluated for GTFs and SGTFs photocatalysts for 532 nm laser and xenon light sources. All measurements were repeated three times and the average was taken.

Photo-degradation of industrial wastewater

In order to evaluate the applicability of our proposed method, it was applied to the degradation of organic materials in textile wastewater samples collected from a textile factory in Zanjan, Iran.

In these experiments, 50 mg of each GTF5/SGTF3 was added separately to a 100 mL beaker containing 50 mL of textile wastewater and subjected to the irradiation by 532 nm laser and xenon light source, respectively for 60 min. Dark adsorption experiments were performed for 30 min, before visible light irradiation, to achieve adsorption-desorption equilibrium. The photocatalysts were separated by applying an external magnet at the bottom of the beakers after 60 min and the upper solutions were collected and transferred for UV-Vis analysis.

RESULTS AND DISCUSSION

Synthesis of photocatalysts

The aim of this research was preparation and evaluation of recoverable and efficient TiO_2-based photocatalysts for degradation of wastewater pollutant. Hence, magnetic NPs were used as the core of these photocatalysts to give them a convenient magnetic separation property. On the other hand, Au and Ag NPs were introduced to the prepared magnetic catalysts to increase their absorption efficiency. For this purpose, a remarkable laser reduction technique was used which is a bottom-up approach in comparison to the approach of laser ablation of bulk materials in solution for producing NPs. We have also tried to use the advantage of this localized heating process to prepare Au-Ag alloys with the aid of

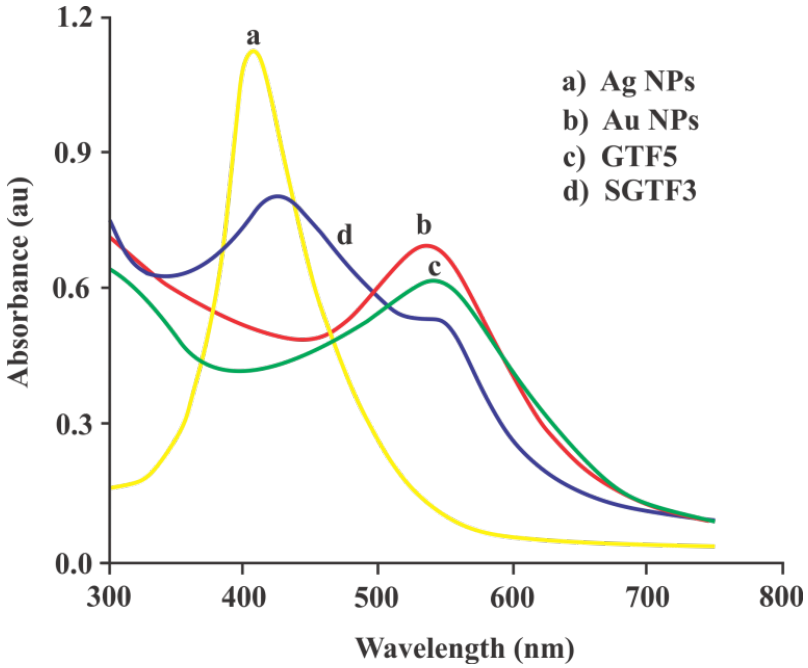

Fig. 1. The UV-Vis spectra of (a) Au NPs, (b) Ag NPs, (c) GTF5 and (d) SGTF3.

the intense nanosecond laser pulses to generate optical breakdown of target-ions containing medium following the generation of free radicals responsible for reduction process of plasmonic metal ions onto the magnetic TiO_2 surface. The results show that prepared NPs have had broad optical absorption band in visible region with efficient catalytic performance.

Characterization of the photocatalysts

Evaluation of LSPR properties

Pure Au and Ag NPs have single LSPR absorption band depends on the size, shape and dielectric characteristics of local environment [37] whereas Ag-Au alloys bi-metallic NPs reveal broad absorption band with two specific maxima in wavelengths which vary with shell thickness of Ag NPs. The UV-Vis spectra of Au and Ag NPs solutions and the as-prepared GTF5 and SGTF3 photocatalysts are shown in Fig. 1. As seen, the LSPR of Au NPs colloidal solution shows a single absorption band around 535 nm, whereas Ag NPs reveals a LSPR band at 405 nm. Decoration of Au NPs onto the surface of TF NPs core was produced a band with a red shift to 560 nm in GTF5 with respect to the pure Au NPs. After decorating GTF5 with Ag NPs, two absorption bands were produced with maximum shift to 549 nm and 420 nm with respect to the pure mono-metallic NPs, respectively. The observed shifts in absorption band are corresponded to the collective nature of Au and Ag NPs LSPR [38] and the converged LSPR of SGTF3 photocatalyst is closer to the surface plasmon wavelength of the pure Ag NPs due to the larger extinction cross-section of Ag. In addition, Figs. 2 and 3 were revealed the change in LSPR of GTF1 to GTF5 and SGTF1 to SGTF3 photocatalysts respectively. Fig. 2 shows that by increasing in the number of pulses applied for reduction of Au ions, the LSPR absorption bands of the photocatalysts are shifted and reached to the maximum of 560 nm in GTF5 and its intensity is increased considerably. By applying Ag NPs to this photocatalyst, two SPR absorption bands were produced at around 420 nm and 549 nm (Fig. 3), corresponding to Ag-Au alloy. It has also been observed that by applying more pulses, the SPR absorption intensity corresponding to the Au NPs has been suppressed and SPR band of Ag NPs became more dominant and slightly shifted to the higher wavelengths due to the increase in NPs volume and also due to the dielectric properties of plasmonic shell.

Size, morphology and structure evaluations

The TEM images of the prepared Fe_3O_4 NPs and TF, GTF5 and SGTF3 photocatalysts are represented in Fig. 4 in which, the spherical Fe_3O_4 NPs are observed in Fig. 4a with particle size of 7-9 nm in diameter. Due to the strong magnetization property, the particles tend to agglomeration

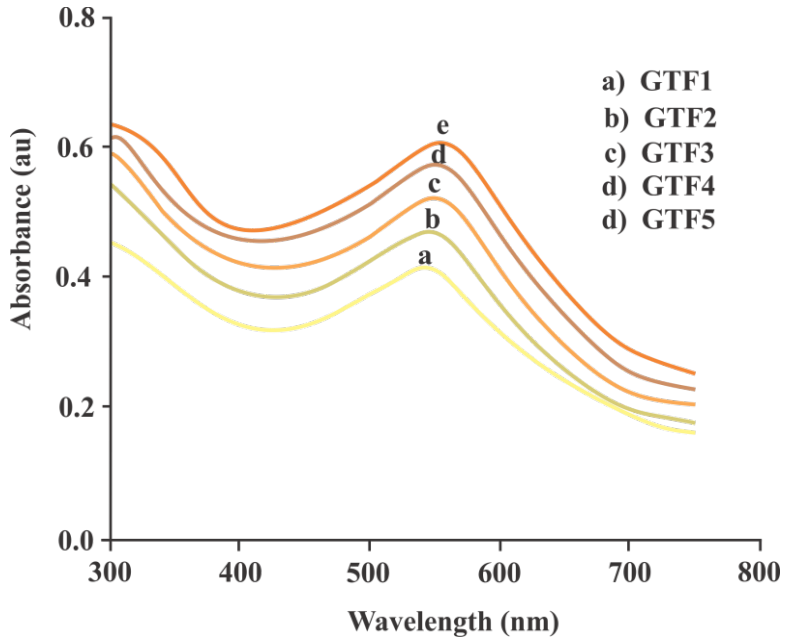

Fig. 2. The change in LSPR of (a) GTF1, (b) GTF2, (c) GTF3, (d) GTF4 and (e) GTF5.

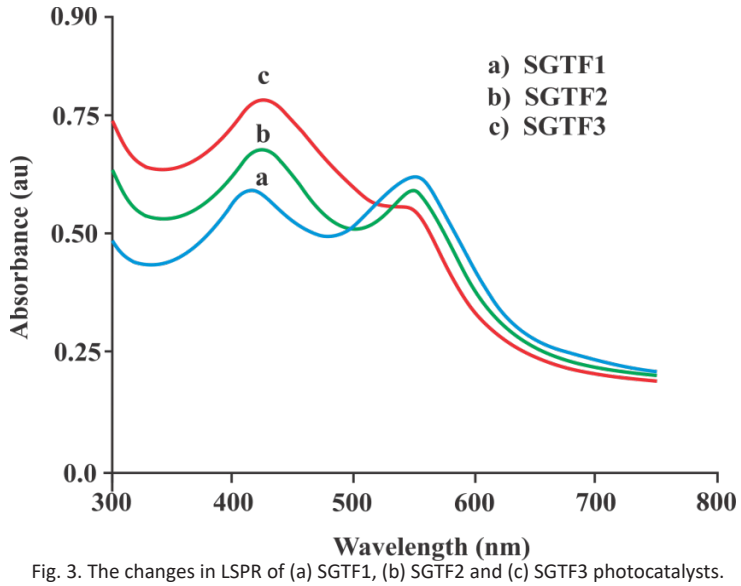

Fig. 3. The changes in LSPR of (a) SGTF1, (b) SGTF2 and (c) SGTF3 photocatalysts.

and thus, were immediately modified with TiO_2 layer. In the procedure of producing TF NPs by vapor-thermal method, the ethanol is evaporated during the heating process because of its low boiling point in compare to the deionized water and also the hydrolysis of TBT. The surface of Fe_3O_4 NPs was acted as the nucleation site and a uniform deposition of TiO_2 layer was constructed on the surface of Fe_3O_4 NPs. As shown in Fig. 4b, the average size of magnetic TiO_2 is increased to 12-14 nm. Fig. 4c represents the TEM image of GTF5 photocatalyst produced by laser-assisted reduction method. Small pure Au NPs are also observed in the image and the average diameter of the photocatalyst was determined to be around 18-20 nm suggesting that the photo-deposition method can be used to produce highly disperse $Au@TiO_2@Fe_3O_4$ NPs. Finally, Fig. 4d shows the TEM image of SGTF3 photocatalyst in which homogeneous alloy NPs with average diameter around 25-30 nm are observed.

The size and morphology of the prepared NPs were further confirmed by SEM analysis. Fig. 5 displays the SEM image of Fe_3O_4 NPs and TF, GTF5 and SGTF3 photocatalysts. All the images show that the core-shell NPs are semi-spherical in shape and randomly distributed. The particle size of the NPs was analyzed using ImageJ software and was in agreement with TEM images.

Crystal structure characterizations

Fig. 6 a-d represents the XRD patterns of Fe_3O_4 NPs and TF, GTF5 and SGTF3 photocatalysts, respectively as peak positions (2θ) in the range of 10-70º. From Fig. 6a, the diffraction peaks at peak position of 30.01º, 36.5º, 43.3º, 53.7 º, 57.8º and 62.8º that are assigned respectively to the reflection planes of (220), (311), (400), (422), (511) and (440) are corresponded to the bulk Fe_3O_4 (JCPDS card No. 19-629) (39). The peaks are sharp and intense, demonstrating well crystallized NPs with cubic inverse spinel structure. Fig. 6b represents the XRD pattern of TF core-shell NPs and demonstrates the diffraction pattern 2θ of 25.1º, 38.1 º, 48.9º, 55.2º, 56.3º, and 62.3º corresponding to the reflection planes of (101), (004), (200), (105), (211), and (204), respectively for TiO_2 layer represents anatase tetragonal structure (JCPDS card No. 21-1272) [39]. All diffraction peaks of Fe_3O_4 NPs core are also observed in the pattern which reveal good crystalinity of the prepared core-shell structure. The XRD patterns of GTF5 and SGTF3 photocatalysts were also demonstrated in Fig. 6c and d. The characteristic diffraction peaks of Au and Ag NPs corresponding to reflection planes of (111), (200), (220), are located at 2θ of 38.77º, 44.33º, 65.62º respectively (JCPDS 01-1174) [38]. Since the space lattice of Au and Ag planes is completely matched with each other, their diffraction patterns were the same. Thus, their peaks were overlapped and there is no obvious difference in their XRD patterns. The obtained results were confirmed the successful synthesis of all core-shell photocatalysts.

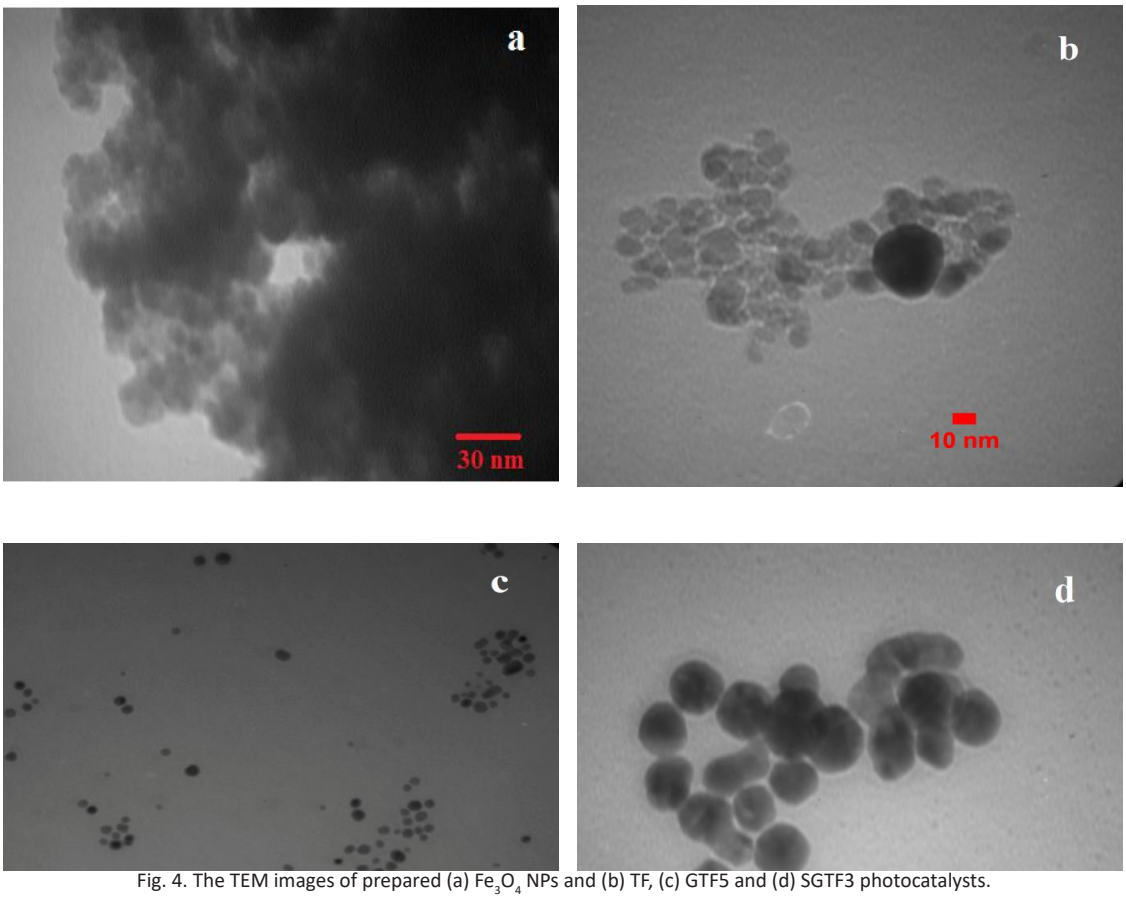

Fig. 4. The TEM images of prepared (a) Fe_3O_4 NPs and (b) TF, (c) GTF5 and (d) SGTF3 photocatalysts.

Magnetic properties

As mentioned before, magnetization property is the key parameter to produce recoverable photocatalysts. The magnetic property of as-prepared Fe_3O_4 NPs and TF, GTF5 and SGTF3 photocatalysts were evaluated at room temperature and the results are displayed in Fig. 7. The results reveal that the magnetic saturation value of the samples is closely related to the thickness of nonmagnetic shells in applied external magnetic field. The saturation magnetization values of Fe_3O_4 NPs and, TF, GTF5 and SGTF3 photocatalysts were obtained around 47.1, 37.8, 24.5 and 20.4 emu g^{-1}, respectively. This reduction in magnetic moment confirms that the size of the non-magnetic layer is increased due to the presence of non-magnetic TiO_2 and plasmonic NPs shells, resulting in a lower magnetic saturation. Since, the decrease in magnetic saturation was low and more importantly, the as-prepared materials exhibited neither coercivity nor remnant magnetization; it can be concluded that the as-prepared magnetic photocatalysts can be demagnetized easily. When external magnetic field decreases to zero, the residual magnetization of the photocatalysts also drops to zero quickly. This is in favor of removal and demagnetization of photocatalysts and provides the feasibility of recovery and reuse-ability of them.

Photocatalytic evaluations of the photocatalysts

The photocatalytic activity of as-prepared photocatalysts was evaluated by measuring photodegradation of MO molecules under irradiation of a 532 nm diode laser and a continuous xenon light source in Vis-NIR region and this dye was selected as a typical degradation target because of its mutagenic nature and high persistency in wastewater [18]. The mineralization and decolorization are the most important mechanisms of organic-dyes photo-degradation in the presence of semiconductor oxides like TiO_2. In the first mechanism, conversion of dye to carbon dioxide and char and in the second mechanism,

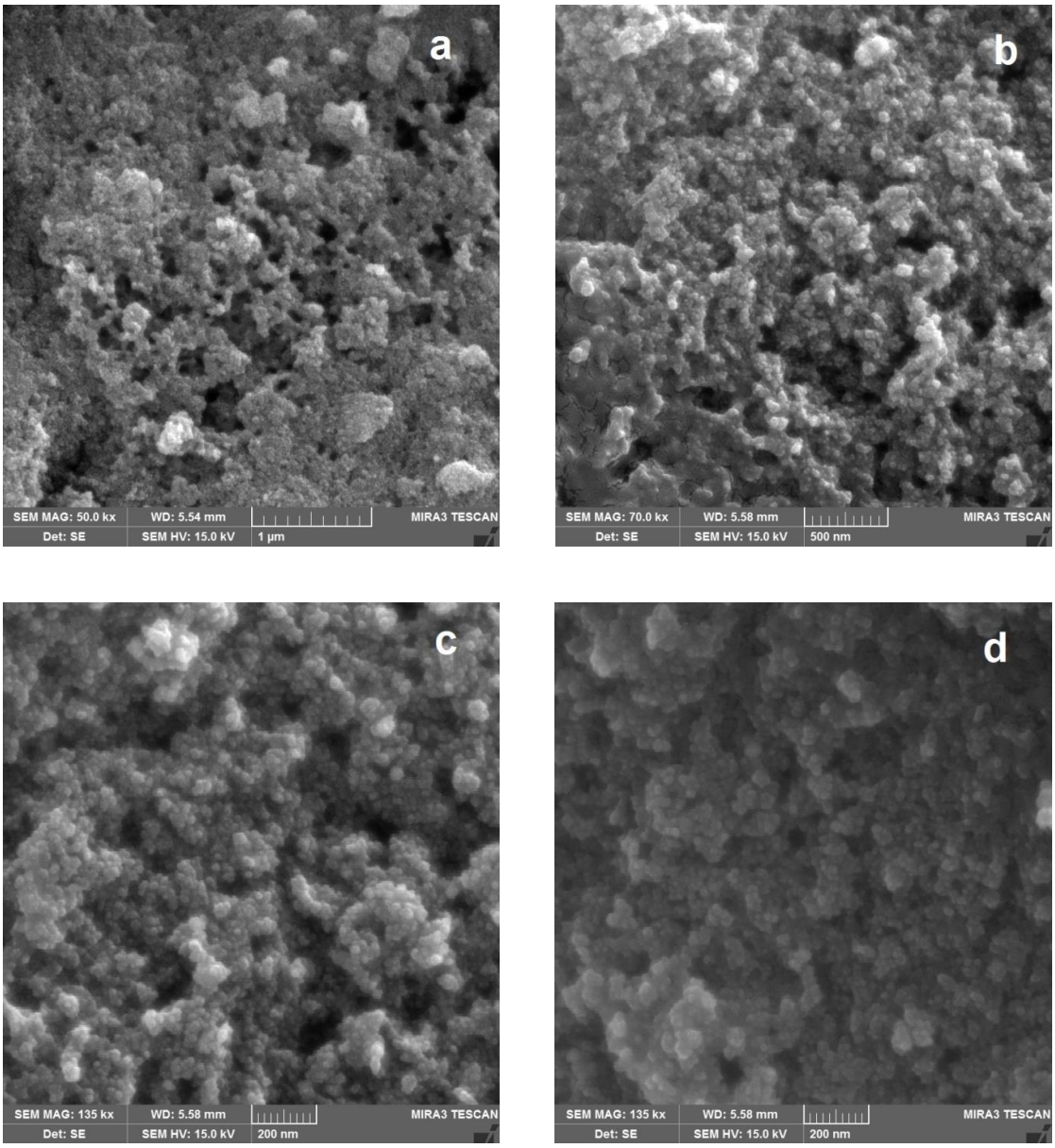

Fig. 5. The SEM images of prepared (a) Fe_3O_4 NPs and (b) TF, (c) GTF5 and (d) SGTF3 photocatalysts.

its conversion to the stable and lower conjugation materials can occur [40, 41].

The photocatalytic reactions were carried out in three steps. At first, the radiation of dye solution (30 mL, concentration= 6×10^{-5} M, pH=4) was performed by applying both laser and xenon light sources for 60 min in absence of photocatalysts to evaluate MO self-degradation. In the second step, dye solutions and the photocatalysts were shaked in a dark place for 30 min to reach adsorption equilibrium and finally, the dye solutions were irradiating in the presence of eight photocatalysts by applying the two above-mentioned light sources. It is necessary to mention that all the MO solutions were irradiated under the same conditions to ensure a reliable comparison of different samples. In addition, the temperature of sample solutions was kept about 30°C during irradiation using a water bath to eliminate thermal effects as a primary cause of degradation. The obtained results revealed that if no photocatalysts was present, the degradation

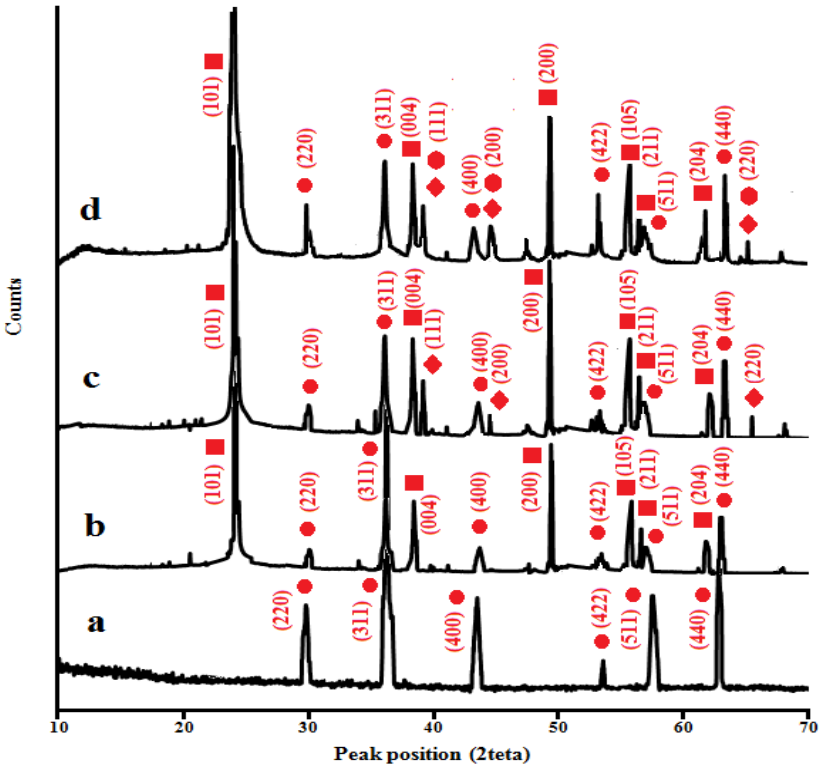

Fig. 6. The XRD patterns of prepared (a) Fe_3O_4 NPs and (b) TF, (c) GTF5 and (d) SGTF3 photocatalysts.

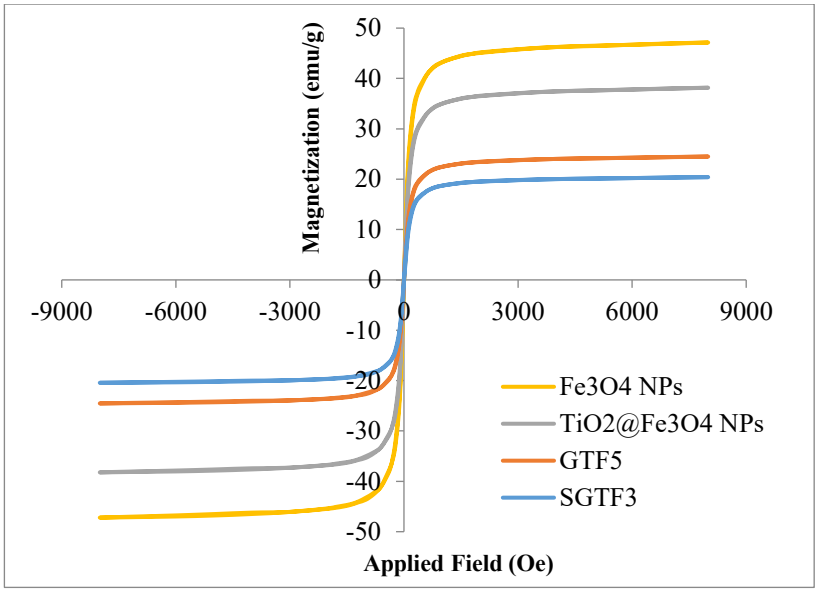

Fig. 7. The magnetization property of prepared (a) Fe_3O_4 NPs and (b) TF, (c) GTF5 and (d) SGTF3 photocatalysts.

of MO was about 6 and 10 % in the presence of 532 nm laser and xenon lamp, respectively in 60 min which is almost very low. The time-dependent photocatalytic degradations of MO solutions by the prepared photocatalysts were represented in Fig. 8 and as can be seen, in the presence of both

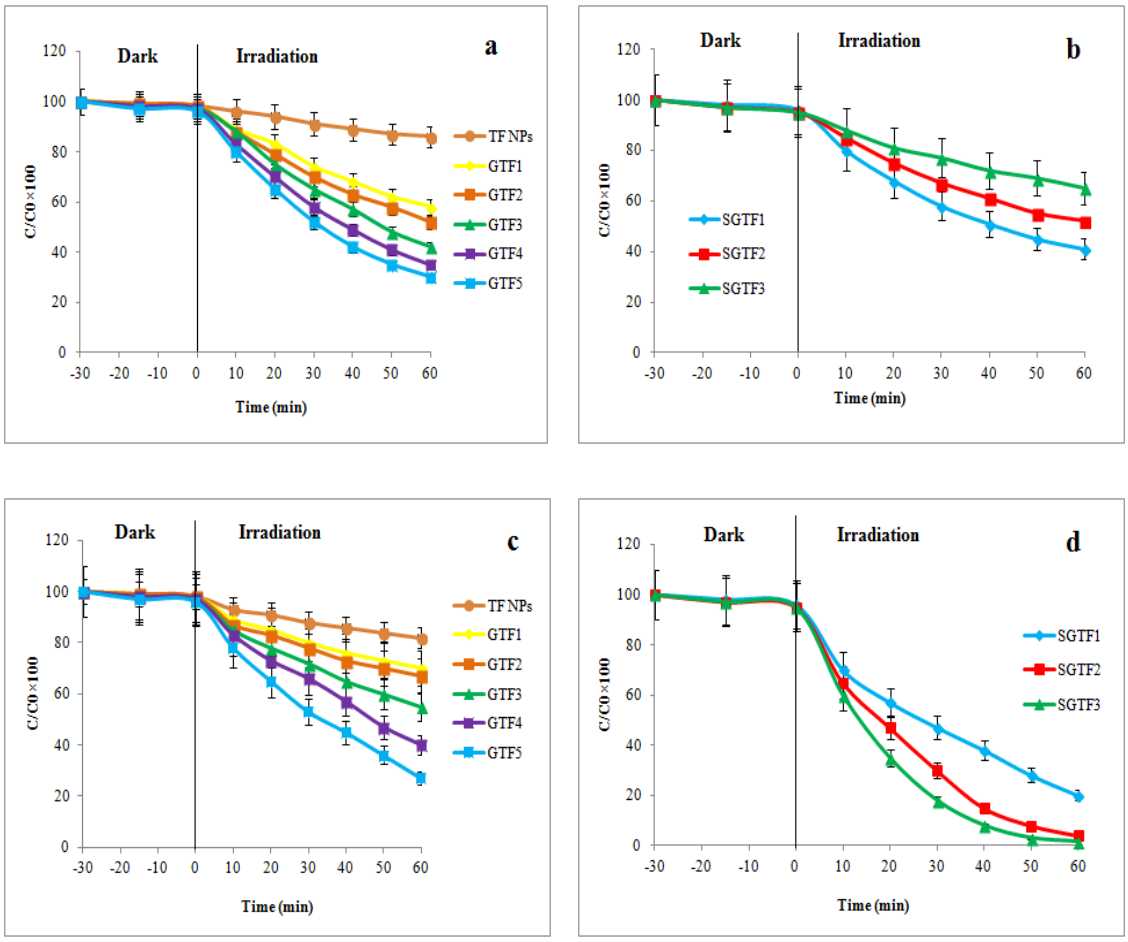

Fig. 8 . Time-dependent photocatalytic degradation of MO using (a) TF and GTF1 to GTF5 photocatalysts in the presence of 532-nm laser, (b) SGTF1 to SGTF3 photocatalysts in the presence of 532-nm laser, (c) TF and GTF1 to GTF5 photocatalysts in the presence of xenon light source, (d) SGTF1 to SGTF3 photocatalysts in the presence of xenon light source.

photocatalysts and visible light, the degradation ratio was increased dramatically and different DR% were achieved depending on the type of photocatalyst and light source applied in the experiment. With 532 nm laser, the DR of TF NPs was low and reached the maximum 89% in 60 min. While, by applying Au NPs at the surface of the photocatalyst, the degradation rate was increased and the DR% values reached about 30% for GTF5. On the other hand, decorating GTF5 with Ag NPs caused a decrease in the degradation rate and an increase in DR% values of the photocatalysts from about 30% in GTF5 to about 41%, 52% and 65% in SGTF1, SGTF2 and SGTF3, respectively. These results are expected when the 532 nm laser was used as the light source because adding Ag NPs to the photocatalysts causes a decrease in the SPR absorption at 532 nm as can also be seen in Fig. 1. In other word, higher Ag shell thickness suppresses the electron transfer from Au NPs core because the SPR of Ag shell which is in another wavelength, starts dominating. Thus, the degradation rate decreases and DR% value increases. From the results, it can be concluded that GTF5 is the most efficient photocatalyst among the prepared photocatalysts when irradiating with 532 nm laser. In addition, all photocatalytic reactions follow the Langmuir-Hinshelwood adsorption model as shown in Fig. 9a and b. The photocatalytic rate constants and half-life times of different photocatalysts were summarized in table 1 and the obtained data was further confirmed the results obtained for degradation rate and DR% in this situation.

However, the results for MO degradation when irradiated by xenon lamp were a little different and summarized in Fig. 8c and d. Generally, the intensity of continuous light sources is much lower

in comparison to a laser for each wavelength. But, the presence of bi-plasmonic NPs gives the photocatalysts higher absorption characteristics in wider wavelength range. Hence, in spite of using laser as a light source, Ag decorated photocatalysts have shown lower DR% value and higher degradation rate. As can be seen from Fig. 8 c and d, a decrease in DR% value was observed from GTF1 to SGTF3 and almost all MO molecules was degraded in 60 min with using SGTF3 as the photocatalysts. Hence, it was considered as the most efficient photocatalyst for degradation of MO solution in the presence of the xenon lamp. The results for Langmuir-Hinshelwood adsorption model in the presence of the continuous light source were summarized in Fig. 9c and d and table 2. As can be seen, the photocatalytic rate constant was increased and $t_{1/2}$ was decreased from GTF1 to SGTF3 which are in good agreement with the data obtained for DR% values.

As mentioned before, TiO_2 semiconductor is known to have low photocatalytic activity under visible light and improvement of its performance is obvious when modified with Au and Ag-Au NPs. This phenomenon is mainly related to the charge transfer and the plasmon resonance energy transfer (PRET) from these plasmonic NPs to TiO_2. The Au and Ag-Au NPs can excite through plasmonic absorption under visible light and the photo-generated electrons were transferred from these NPs to the C_B of TiO_2, resulting in efficient e^-/h^+ separation and oxidation of MO on the surfaces of the photocatalysts. The MO degradation mechanism involves the cleavage of azo bond, successive demetylation/addition of hydroxyl groups to rings and cleavage of sulphonate group from the ring (Fig. 10) [42].

Effect of pH

One of the critical parameters in photocatalytic

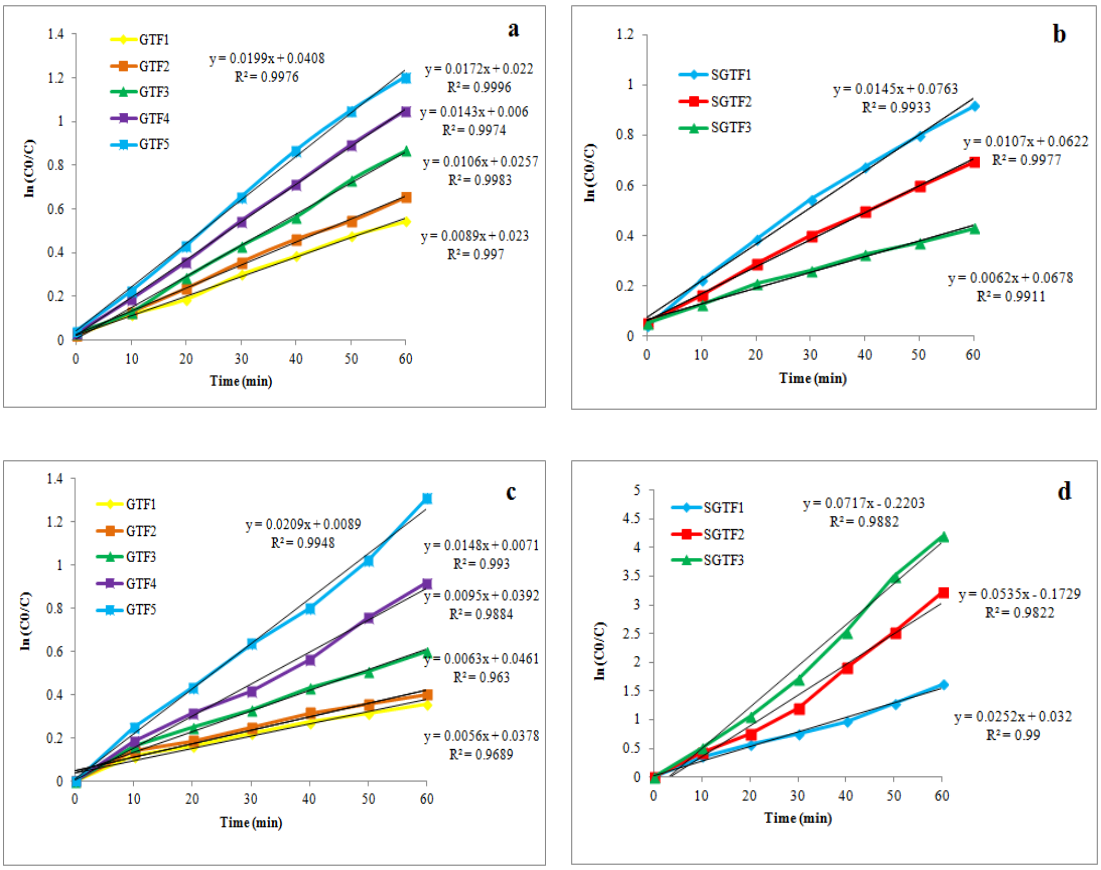

Fig. 9. Kinetics of photodegradation of MO using (a) TF and GTF1 to GTF5 photocatalysts in the presence of 532-nm laser, (b) SGTF1 to SGTF3 photocatalysts in the presence of 532-nm laser, (c) TF and GTF1 to GTF5 photocatalysts in the presence of xenon light source, (d) SGTF1 to SGTF3 photocatalysts in the presence of xenon light source.

Table 1. Results for evaluation of kinetic parameters of MO degradation using GTF1 to GTF5 and SGTF1 to SGTF3 photocatalysts irradiated by a 532 nm laser.

Photocatalyst	Equation	R^2	k	$t_{1/2}$
GTF1	y = 0.0089x + 0.023	0.997	0.0089	77.88
GTF2	y = 0.0106x + 0.0257	0.998	0.0106	65.39
GTF3	y = 0.0143x + 0.006	0.997	0.0143	49.51
GTF4	y = 0.0172x + 0.022	0.999	0.0172	40.30
GTF5	y = 0.0199x + 0.0408	0.998	0.0199	34.83
SGTF1	y = 0.0145x + 0.0763	0.993	0.0145	47.80
SGTF2	y = 0.0107x + 0.0622	0.998	0.0107	64.78
SGTF3	y = 0.0062x + 0.0678	0.991	0.0062	111.80

Table 2. Results for evaluation of kinetic parameters of MO degradation using GTF1 to GTF5 and SGTF1 to SGTF3 photocatalysts irradiated by a continuous xenon light source.

Photocatalyst	Equation	R^2	k	$t_{1/2}$
GTF1	y = 0.0056x + 0.0378	0.969	0.0056	123.77
GTF2	y = 0.0063x + 0.0461	0.963	0.0063	110.02
GTF3	y = 0.0095x + 0.0392	0.988	0.0095	72.96
GTF4	y = 0.0148x + 0.0071	0.993	0.0148	46.83
GTF5	y = 0.0209x + 0.0089	0.995	0.0209	33.16
SGTF1	y = 0.0252x + 0.032	0.990	0.0252	27.50
SGTF2	y = 0.0535x - 0.1729	0.982	0.0535	12.95
SGTF3	y = 0.0717x - 0.2203	0.988	0.0717	9.66

degradation of dye molecules is pH because it can affect on dye adsorption on the photocatalyst. In addition, surface charge of the catalyst can also be influenced by pH of solution and can be evaluated by considering a parameter named the point of zero charge (PZC). Thus, the effect of initial pH value of dye solution on the degradation of MO molecules was studied in the range of 2-9 and the results are shown in Fig. 11. The prepared GTF5 and SGTF3 with pH_{PZC} in the range of 6-7 (data are not shown here) were considered as the optimum photocatalysts for performing the experiments with the 532 nm laser and xenon light sources, respectively. MO molecule is known to has anionic nature with pK_a=3.4. Thus, in pH values above this pK_a, the electrostatic attraction between the photocatalysts and MO molecules is favor of its adsorption to the catalyst surface because in $pH<pH_{PZC}$ ranges, the photocatalysts have positively charged surface. In pH values below the pK_a, concentration of H^+ is high and MO surface becomes positive which leads to low adsorption of MO to the catalyst surface and low degradation efficiency. On the other hand, an increase in %degradation was also observed in higher pH as shown in the figure. It is known that at high pH, the $OH^•$ radicals are largely responsible for oxidation process [43] because these radicals play an essential role in the cleavage of N=N conjugated system in azo dyes [41] which is led to higher degree of dye degradation.

Reusability of the photocatalysts

As discussed before, one of the main advantages of the prepared photocatalysts is their recyclability which give them reusability property. In this manner, all GTFs and SGTFs photocatalysts which suspended in the dye solution can be easily

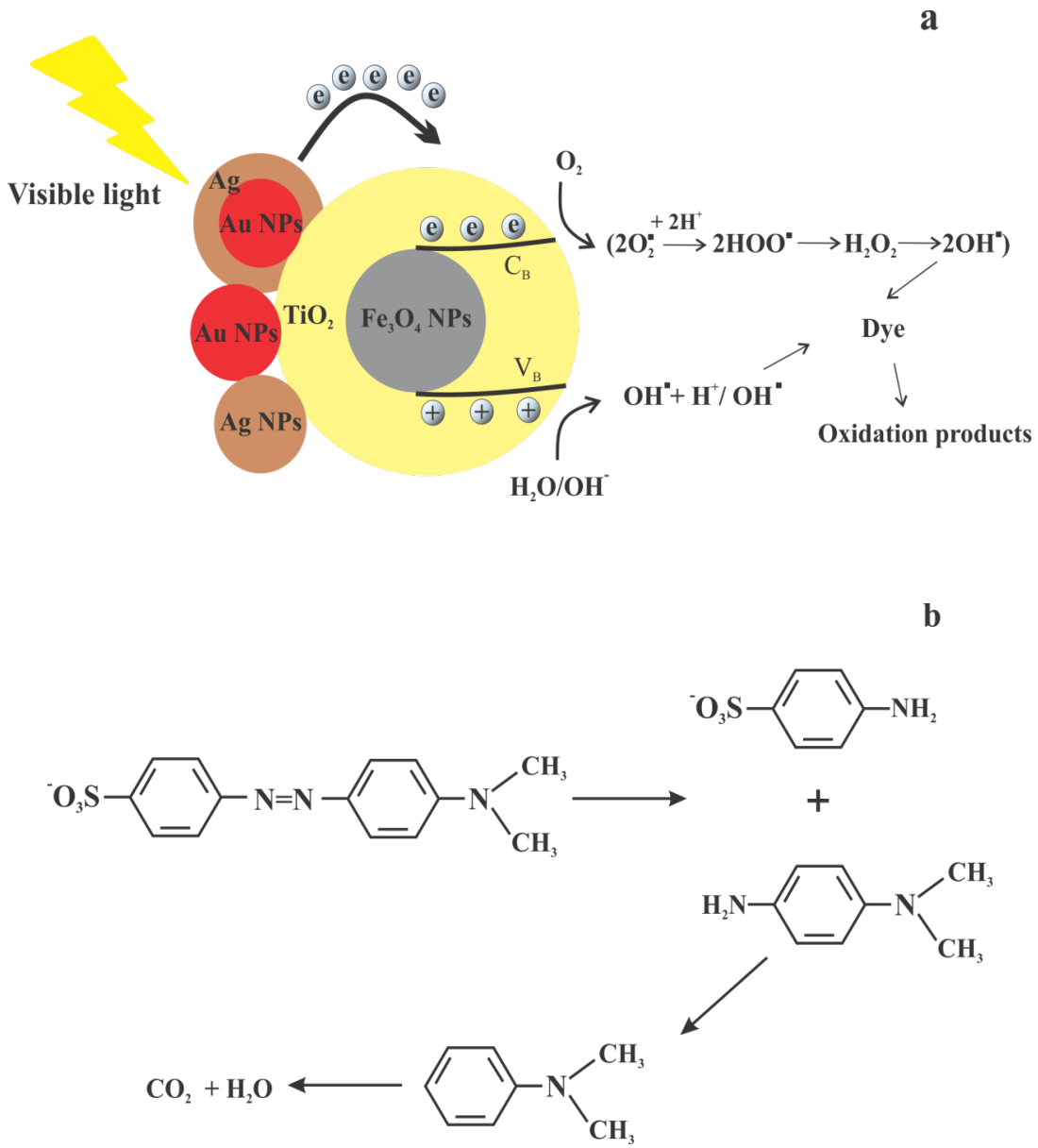

Fig. 10. The photo-degradation of MO (a) schematic of the procedure and (b) products of degradation.

withdrawn using an external supermagnet like NdFeB. When the magnet is placed under the flask, the photocatalysts attract to the bottom of the flask in only one minute and can be easily separated from the upper solution.

In these experiments, the superiority of GTF5 and SGTF3 photocatalysts was examined by evaluating their catalytic activity in five successive cycles. The recovered photocatalysts were washed with ethanol (25 mL, twice) and deionized water (25 mL, three times) and dried in vacuum oven at 50 ºC for further degradation experiments. The relative standard deviation (RSD%) of DR% after 60 min was used to evaluate the reusability. The obtained results revealed that the photocatalytic activity of the photocatalysts was not considerably changed (RSD< 7%) which means that the prepared magnetically recoverable photocatalysts are stable and effective for the degradation of polluted water.

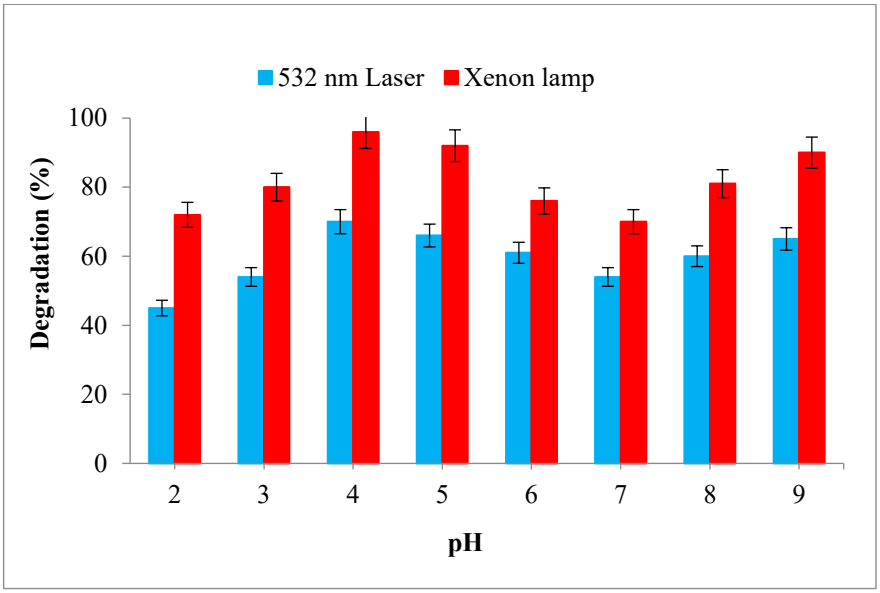

Fig. 11. Effect of pH on the degradation of MO solutions in the presence of GTF5 and SGTF3 photocatalysts using 532 nm laser and xenon light source, respectively.

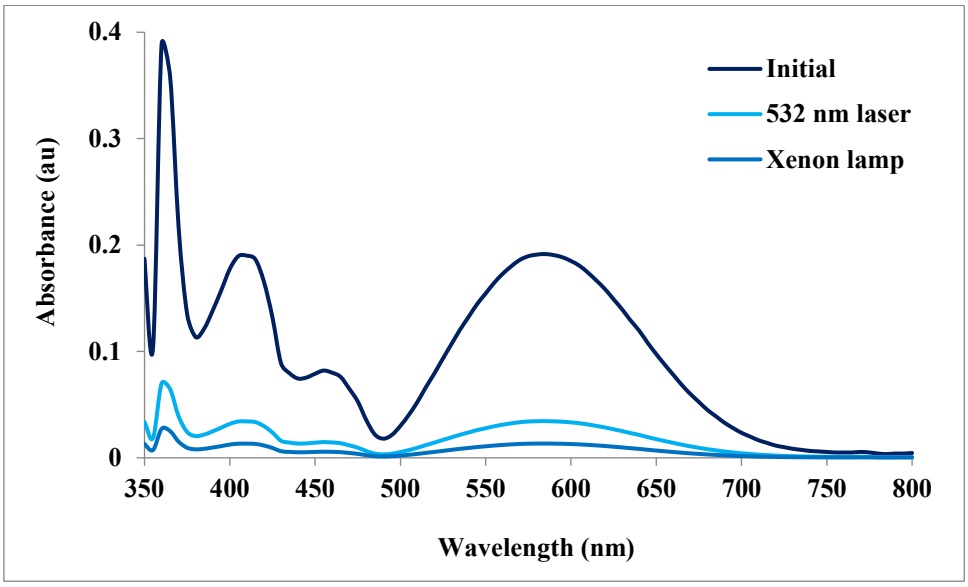

Fig. 12. The UV-Vis spectra of initial textile wastewater before and after treating with 532-nm laser and xenon lamp in the presence of GTF5 and SGTF3 photocatalysts, respectively.

Photodegradation of industrial wastewater

In order to evaluate the applicability of proposed method, it was applied to the degradation of organic molecules in textile wastewater samples. Because of the wide variety of processing steps, textile wastewaters typically contain a complex mixture of organic and inorganic chemicals. Fig. 12 represents the UV-Vis spectrum of the collected wastewater and it can be seen that multiple absorption bands are initially existed in the spectrum such as an intense broad absorption band around 590 nm and several bands around 460 nm, 410 nm and 360 nm. In the presence of photocatalysts and visible light irradiation, the intensity of all the bands was decreased dramatically after 60 min and almost no

absorbance remained between 450 nm and 500 nm when the sample was treated with xenon light source. The obtained results revealed that the as-prepared photocatalysts have great potential for photocatalytic activity in visible light with high degradation efficiency and shows reusable character after several treatment cycles.

CONCLUSIONS

In this research, novel multifunctional magneto-plasmonic TiO_2 nanocatalysts with different amount of Au and Ag shell thickness were successfully synthesized and applied for degradation of MO dye as a model wastewater pollutant. Two kinds of light sources including a linear high-intensity laser with the wavelength of 532 nm and a continuous xenon light source in the Vis-NIR range were examined and it was demonstrated that the photocatalytic activity of the nanocatalysts can be influenced by the plasmonic shell thickness and type of light source applied in the experiments. The kinetics and mechanism of MO degradation were investigated and it also was revealed that due to their excellent catalytic and magnetic properties, the photocatalysts can be re-used for several cycles with convenient magnetic separability without sacrificing their efficiency. The applicability of the photocatalysts was further confirmed by application of the method for degradation of organic materials in textile wastewater.

CONFLICT OF INTEREST

The authors declare that there is no conflict of interests regarding the publication of this manuscript.

REFERENCES

1. D'Amato CA, Giovannetti R, Zannotti M, Rommozzi E, Ferraro S, Seghetti C, et al. Enhancement of visible-light photoactivity by polypropylene coated plasmonic Au/TiO2 for dye degradation in water solution. Applied Surface Science. 2018;441:575-87.
2. Colmenares JC, Luque R. Heterogeneous photocatalytic nanomaterials: prospects and challenges in selective transformations of biomass-derived compounds. Chemical Society Reviews. 2014;43(3):765-78.
3. Huy TH, Bui DP, Kang F, Wang Y-F, Liu S-H, Thi CM, et al. SnO_2/TiO_2 nanotube heterojunction: The first investigation of NO degradation by visible light-driven photocatalysis. Chemosphere. 2019;215:323-32.
4. Greene D, Serrano-Garcia R, Govan J, Gun'ko YK. Synthesis Characterization and Photocatalytic Studies of Cobalt Ferrite-Silica-Titania Nanocomposites. Nanomaterials. 2014;4(2):331-43.
5. Kisch H. Semiconductor photocatalysis--mechanistic and synthetic aspects. Angewandte Chemie (International ed in English). 2013;52(3):812-47.
6. Hong S, Ratpukdi T, Sungthong B, Sivaguru J, Khan E. A sustainable solution for removal of glutaraldehyde in saline water with visible light photocatalysis. Chemosphere. 2019;220:1083-90.
7. Wu Q, Que Z, Li Z, Chen S, Zhang W, Yin K, et al. Photodegradation of ciprofloxacin adsorbed in the intracrystalline space of montmorillonite. Journal of Hazardous Materials. 2018;359:414-20.
8. Etminan M, Nabiyouni G, Ghanbari D, Preparation of tin ferrite–tin oxide by hydrothermal, precipitation and auto-combustion: photo-catalyst and magnetic nanocomposites for degradation of toxic azo-dyes. J Mater Sci: Mater Electron 2018; 29: 1766–1776.
9. Eskandari N, Nabiyouni Gh, Masoumi Sh, Ghanbari D, Preparation of a new magnetic and photo-catalyst $CoFe_2O_4$–SrTiO3 perovskite nanocomposite for photo-degradation of toxic dyes under short time visible irradiation. Composites Part B: Engineering 2019; 176: 107343.
10. Bagheri A, Halakouie H, Ghanbari D, Mousayi M., Asiabani N, Strontium hexa-ferrites and polyaniline nanocomposite: Studies of magnetization, coercivity, morphology and microwave absorption. Journal of Nanostructures 2019; 9: 630-638.
11. Sorinezami Z, Ghanbari D, Facile preparation of silver nanoparticles and antibacterial Chitosan-Ag polymeric nanocomposites. Journal of Nanostructures 2019; 9: 396-401.
12. Nabiyouni Gh, Ghanbari D, Simple preparation of magnetic, antibacterial and photo-catalyst $NiFe_2O_4$@TiO_2/Pt nanocomposites. Journal of Nanostructures 2018; 8: 408-416.
13. Bricchi BR, Ghidelli M, Mascaretti L, Zapelli A, Russo V, Casari CS, et al. Integration of plasmonic Au nanoparticles in TiO_2 hierarchical structures in a single-step pulsed laser co-deposition. Materials & Design. 2018;156:311-9.
14. Stefan M, Pana O, Leostean C, Bele C, Silipas D, Senila M, et al. Synthesis and characterization of Fe_3O_4–TiO_2 core-shell nanoparticles. Journal of Applied Physics. 2014;116(11):114312.
15. Ma F-P, Li P-H, Li B-L, Mo L-P, Liu N, Kang H-J, et al. A recyclable magnetic nanoparticles supported antimony catalyst for the synthesis of N-substituted pyrroles in water. Applied Catalysis A: General. 2013;457:34-41.
16. Nasir Baig RB, Varma RS. Organic synthesis via magnetic attraction: benign and sustainable protocols using magnetic nanoferrites. Green Chemistry. 2013;15(2):398-417.
17. Baig RBN, Varma RS. Magnetically retrievable catalysts for organic synthesis. Chemical Communications. 2013;49(8):752-70.
18. Ma P, Jiang W, Wang F, Li F, Shen P, Chen M, et al. Synthesis and photocatalytic property of Fe_3O_4@TiO_2 core/shell nanoparticles supported by reduced graphene oxide sheets. Journal of Alloys and Compounds. 2013;578:501-6.
19. Jiménez-Totozintle M, Ferreira IJ, da Silva Duque S, Guimarães Barrocas PR, Saggioro EM. Removal of contaminants of emerging concern (CECs) and antibiotic resistant bacteria in urban wastewater using UVA/TiO_2/H_2O_2 photocatalysis. Chemosphere. 2018;210:449-57.
20. Naldoni A, Riboni F, Guler U, Boltasseva A, Shalaev Vladimir M, Kildishev Alexander V. Solar-Powered Plasmon-Enhanced

Heterogeneous Catalysis. Nanophotonics2016. p. 112.
21. Ahmad J, Majid K. Enhanced visible light driven photocatalytic activity of CdO–graphene oxide heterostructures for the degradation of organic pollutants. New Journal of Chemistry. 2018;42(5):3246-59.
22. Atwater HA, Polman A. Plasmonics for improved photovoltaic devices. Nat Mater. 2010;9.
23. Kochuveedu ST, Jang YH, Kim DH. A study on the mechanism for the interaction of light with noble metal-metal oxide semiconductor nanostructures for various photophysical applications. Chem Soc Rev. 2013;42(21):8467-93.
24. Li H, Bian Z, Zhu J, Huo Y, Li H, Lu Y. Mesoporous Au/TiO2 nanocomposites with enhanced photocatalytic activity. J Am Chem Soc. 2007;129(15):4538-9.
25. Furube A, Du L, Hara K, Katoh R, Tachiya M. Ultrafast Plasmon-Induced Electron Transfer from Gold Nanodots into TiO_2 Nanoparticles. Journal of the American Chemical Society. 2007;129(48):14852-3.
26. Yu K, Tian Y, Tatsuma T. Size effects of gold nanaoparticles on plasmon-induced photocurrents of gold–TiO_2 nanocomposites. Physical Chemistry Chemical Physics. 2006;8(46):5417-20.
27. Kowalska E, Mahaney OO, Abe R, Ohtani B. Visible-light-induced photocatalysis through surface plasmon excitation of gold on titania surfaces. Physical chemistry chemical physics : PCCP. 2010;12(10):2344-55.
28. Mubeen S, Hernandez-Sosa G, Moses D, Lee J, Moskovits M. Plasmonic Photosensitization of a Wide Band Gap Semiconductor: Converting Plasmons to Charge Carriers. Nano Letters. 2011;11(12):5548-52.
29. Fu C, Li M, Li H, Li C, Wu Xg, Yang B. Fabrication of Au nanoparticle/TiO_2 hybrid films for photoelectrocatalytic degradation of methyl orange. Journal of Alloys and Compounds. 2017;692:727-33.
30. Lermé J. Size Evolution of the Surface Plasmon Resonance Damping in Silver Nanoparticles: Confinement and Dielectric Effects. The Journal of Physical Chemistry C. 2011;115(29):14098-110.
31. Brandl DW, Mirin NA, Nordlander P. Plasmon Modes of Nanosphere Trimers and Quadrumers. The Journal of Physical Chemistry B. 2006;110(25):12302-10.
32. Mashhadizadeh MH, Amoli-Diva M. Drug-Carrying Amino Silane Coated Magnetic Nanoparticles as Potential Vehicles for Delivery of Antibiotics. J Nanomed Nanotechol. 2012;3(4):139-46.
33. Mashhadizadeh MH, Amoli-Diva M, Pourghazi K. Magnetic nanoparticles solid phase extraction for determination of ochratoxin A in cereals using high-performance liquid chromatography with fluorescence detection. Journal of Chromatography A. 2013;1320(0):17-26.
34. Jia K, Yuan L, Zhou X, Pan L, Wang P, Chen W, et al. One-pot synthesis of Au/Ag bimetallic nanoparticles to modulate the emission of CdSe/CdS quantum dots. RSC Advances. 2015;5(72):58163-70.
35. Lee C-H, Shie J-L, Yang Y-T, Chang C-Y. Photoelectrochemical characteristics, photodegradation and kinetics of metal and non-metal elements co-doped photocatalyst for pollution removal. Chemical Engineering Journal. 2016;303:477-88.
36. Zhuo S, Shao M, Lee S-T. Upconversion and Downconversion Fluorescent Graphene Quantum Dots: Ultrasonic Preparation and Photocatalysis. ACS Nano. 2012;6(2):1059-64.
37. Misra M, Gupta RK, Paul AK, Singla M. Influence of gold core concentration on visible photocatalytic activity of gold–zinc sulfide core–shell nanoparticle. Journal of Power Sources. 2015;294:580-7.
38. Misra M, Singh N, Gupta RK. Enhanced visible-light-driven photocatalytic activity of Au@Ag core–shell bimetallic nanoparticles immobilized on electrospun TiO_2 nanofibers for degradation of organic compounds. Catalysis Science & Technology. 2017;7(3):570-80.
39. Hasanpour A, Niyaifar M, Mohammadpour H, Amighian J. A novel non-thermal process of TiO_2-shell coating on Fe3O4-core nanoparticles. Journal of Physics and Chemistry of Solids. 2012;73(9):1066-70.
40. Yang J, Chen C, Ji H, Ma W, Zhao J. Mechanism of TiO_2-Assisted Photocatalytic Degradation of Dyes under Visible Irradiation: Photoelectrocatalytic Study by TiO2-Film Electrodes. The Journal of Physical Chemistry B. 2005;109(46):21900-7.
41. Ajmal A, Majeed I, Malik RN, Idriss H, Nadeem MA. Principles and mechanisms of photocatalytic dye degradation on TiO_2 based photocatalysts: a comparative overview. RSC Advances. 2014;4(70):37003-26.
42. Xie S, Huang P, Kruzic JJ, Zeng X, Qian H. A highly efficient degradation mechanism of methyl orange using Fe-based metallic glass powders. Scientific Reports. 2016;6:21947.
43. Tunesi S, Anderson M. Influence of chemisorption on the photodecomposition of salicylic acid and related compounds using suspended titania ceramic membranes. The Journal of Physical Chemistry. 1991;95(8):3399-405.